Coastal Engineering 180 (2023) 104254

Contents lists available at ScienceDirect

Coastal Engineering

journal homepage: www.elsevier.com/locate/coastaleng

Laboratory measurements of mean and turbulence velocities and shear stresses through the wave roller in strong plunging waves

K. Govender [a,*], R. Mukaro [b], G. Mocke [c]

[a] Cape Peninsula University of Technology, Symphony Way, Bellville, Cape Town, 7535, Western Cape, South Africa
[b] North West University, North West Province, South Africa
[c] Advisian, Madrid, Spain

ARTICLE INFO

Keywords:
Bubble image
Inner and outer surf zones
Mass and velocity fluxes
Plunging wave
Shear stress
Turbulence intensities
Undertow

ABSTRACT

In this paper we present experimental measurements of mean and turbulent velocities in a strongly plunging wave. Measurement of the fluid velocities over the entire water column and through the outer and inner surf zones were obtained by particle and bubble image velocimetry. The velocity flow fields were analyzed to estimate mean and turbulent velocity by Reynolds decomposition. The mean velocities were used to estimate the forward and reverse mass fluxes, from which an estimate of the average fluid density in crest of the waves is obtained. In addition we provide details of the wave and turbulent shear stresses. The changes in characteristics of all these quantities as the wave propagates from the break point into the outer and inner surf zones are highlighted. We provide observations of both time dependent and phase averaged features of velocities, turbulence kinetic energy (TKE), and the wave and turbulence shear stresses over the wave cycle. The average relative fluid density in the wave crests was found to have an upper bound between 20 % in the outer surf zone to 30 % in the inner surf zone. This translates to a lower bound for the void fraction of approximately 0.8 and 0.7 in the outer and inner zones, respectively. The measured wave shear stress was found to be of similar magnitudes as the turbulence shear stress. The wave shear stress also changed sign depending on the horizontal position along the surf zone and on the relative phases between the horizontal and vertical velocities. For this particular wave conditions the measured Froude scaled TKE was found to be higher than those previously reported in the literature. Near the bottom, Froude scaled TKE values of approximately 0.1 was observed, while peak values of 0.25 were measured above the trough level.

1. Introduction and background theory

The nearshore region of the ocean is dominated by highly complex nonlinear fluid processes. These processes play a major role in sediment suspension and transport, leading subsequently to beach erosion and coastline changes. These nonlinear processes begin with shoaling of the wave as it moves up a sloping beach, followed by breaking and formation of the roller. The roller then develops into a bore like character as the wave propagates. The horizontal region between the initial point of breaking and the point at which the roller is fully developed represents the outer surf zone, and the region following this is the inner surf zone. In the outer surf zone, the overturning crest in the plunging wave traps large quantities of air, causing large scale aeration structures which penetrate deep into the water column and often reaches the bottom boundary which can stir up huge amounts of sediments. Most of these large scale eddies are also associated with simultaneous presence of large concentration of air bubbles, even below the trough level under the crest and in the trough region, as we will show later. The large scale structures created by the overturning crest can be convected seawards due to the undertow and can persists for a large portion of the wave cycle, extending into the trough region. In the outer surf zone the large scale structures and turbulence are transported mainly by advection, whereas in the inner surf zone, where the roller is fully developed, the turbulence is transported mainly by diffusive processes towards the seabed.

The hydrodynamics of the surf zone have been studied quite extensively since the late ’70s and early ’80s. Early qualitative and geometrical observations of the evolution of wave breaking were conducted by Basco (1985), Jansen (1986) and Bonmarin (1989). More quantitative experiments were conducted using techniques such as LDA (Stive, 1980) and hot film/wire anemometry (Flick et al., 1981) to measure fluid velocities below the trough level in breaking waves. Due to the sensitivity of these techniques to air bubbles, measurements in these cases were limited to positions below the trough level and

* Corresponding author.
E-mail addresses: govenderk@cput.ac.za (K. Govender), Raphael.Mukaro@nwu.ac.za (R. Mukaro), gpmocke@gmail.com (G. Mocke).

https://doi.org/10.1016/j.coastaleng.2022.104254
Received 13 July 2022; Received in revised form 12 September 2022; Accepted 18 November 2022
Available online 29 November 2022

outside the plunging breaker zone. Improvements to the standard LDA were made by the introduction of fiber optic LDA (see for example Nadaoka and Kondoh (1982), Ting and Kirby (1994, 1995)). These methods still experience bubble contamination. They are also point measurements techniques and in order to obtain the flow field over the entire wave, repeated measurements are required. Despite these limitations LDA is still used and continue to provide valuable insight into wave breaking hydrodynamics (Liiv (2001), Stansby and Feng (2005), De Serio and Mossa (2006), Van der A et al. (2017)). These traditional methods are now supplemented using video techniques such as particle image velocimetry (PIV) and bubble image velocimetry (BIV) to provide further insight into hydrodynamics in the upper part of the water column where large concentration of air bubbles exists (see for example Chang and Liu (1996, 1999) and Govender et al. (2002)). Although the use of bubbles as tracers in two phase flows have been reported previously (Hansen et al., 1992), Govender et al. (2002) used video and bubble imaging techniques to produce measurements of velocities and turbulence spanning the entire water column, including the highly aerated crest regions, in both spilling and plunging waves. This was followed by measurements of turbulence dissipation in the wave crests in spilling waves (Govender et al., 2004). Other researchers have also adopted similar techniques (see for example Ryu et al. (2005), Kimmoun and Branger (2007), Na et al. (2016, 2018)).

The higher aeration content in plunging waves makes experimental studies of these wave cases much more difficult, compared to spilling waves, although some success have been made using LDA for positions below the trough level where the concentration of aeration is reduced (Ting and Kirby (1994), Ting and Kirby (1995)). However, it is still considered that these measurements may still be under reading turbulence levels in cases of high aeration content. Other plunging studies using LDA below the trough level include Liiv (2001), Liiv and Lagemaa (2008), and De Serio and Mossa (2006). De Serio and Mossa (2006) reported on velocity and shear stress for three wave cases (including a plunging wave). They showed a phase shift between the orbital horizontal and vertical components that differs from those found in non-breaking waves. In sinusoidal waves this phase shift is $\pi/2$ and in Cnoidal type waves a phase shift of $\pi/4$ is typical. They also indicate that vertical mixing is stronger in the plunging case, and that TKE transport in the plunging wave is seawards and downwards. Liiv (2001), Liiv and Lagemaa (2008) have reported on a mild plunging wave breaking on a smooth 1:17 slope beach. The beach was constructed of vinyl plates. Measurements of the turbulence intensity, turbulent kinetic energy and Reynolds stress were conducted. They showed that large scale motion dominate in turbulence under plunging waves. They also report that turbulent kinetic energy (TKE) reaches a maximum value under the crest of the wave and decreases to a constant value under the wave troughs.

Large scale experiments involving plunging waves breaking on a mild slope 1:100 beach was conducted for positions below the trough level by Hsu et al. (2019). Velocities across the water column was measured using an array of acoustic doppler velocimeters at one horizontal position in the outer surf zone. They showed intermittency of TKE near the bed caused by large scale eddies. Although intermittency has been reported in earlier studies (see for example Cox and Kobayashi (2000), Longo (2009), Huang et al. (2010),Ting (2013) and Ting and Reimnitz (2015)). Hsu et al. (2019) also measured the wave shear stress and reported that this can be up to an order larger than the turbulence shear stress. They also report that the sign of the wave shear stress can change depending on the relative phase of the horizontal and vertical velocity components.

Other experimental studies of plunging waves in laboratory surf zones include Pedrozo-Acuña and Silva (2011), Sou et al. (2010), Ting (2013), Ting and Reimnitz (2015). Pedrozo-Acuña and Silva (2011) investigated the spatial and temporal evolution of the pressure fields and gradients in pressure induced by a plunging wave in the nearshore surf zone. They measured pressure versus time curves and the fluid velocities across the shoaling, breaking and swash zones. Velocities over the entire water column were measured using BIV. Their findings are that the local fluid acceleration in the shoaling and breaking zones can be used to account for the gradients in pressure, which is consistent with their previous studies. Sou et al. (2010) conducted PIV measurements at four positions in the surf and swash zones to examine the evolution of the turbulence and the dissipation and production of isotropic turbulence. Using fluorescent particles they measured velocities over the entire water column. They have identified three temporal regions over the wave phase which characterizes the evolution of turbulence: phases that are associated with the turbulence due to wave breaking and the shear layer, the phases associated with decay and the phases dominated by bed generated turbulence. Also pointed out by Sou et al. (2010), the phase-averaged mean flowfields indicate a shear layer occurs when the uprush due to the bore wave-front interacts with the downwash flow. Ting (2013) conducted PIV measurements in the boundary layer in laboratory waves breaking on a 3% slope to investigate the impact of the vortices generated during impingement. The results showed that the impact of a plunging wave vortex on the bottom was highly transient and 3D in character, consisting of counter rotating vorticity. A transverse vortex formed the lower bend of the vortex loop where it collided with the bottom. Also the impingement region was not stationary but moved shorewards. The 3D characteristics of the vortex was further investigated by Ting and Reimnitz (2015) who conducted 3D velocity measurements using 3 component velocimetry in a plunging wave breaking on a 1:40 slope beach. Measurements were conducted in the outer surf zone to capture the plunger vortex generated due to the incident breaking and the splashup vortex generated at the second plunge point. As mentioned, the basic 3D form of vortex observed was a vortex loop with counter rotating vorticity; two vortices obliquely oriented along the wave propagation direction are connected at the base by a transverse vortex. The measured TKE increased and decreased rapidly during the passing of the down flow and transverse vortex. TKE was transported downwards by turbulence velocities associated with the down flow and transverse vortex.

Another property of breaking waves that is important is the fraction of air entrained during the breaking process. This is usually referred to as the void fraction. There have been a number of measurements of void fraction in the surf zone, as well as in deep water breaking waves. Early measurements of void fractions in the surf zone were conducted using resistive probes (Hwung et al. (1992), Cox and Shin (2003), Hoque and Aoki (2005), Mori et al. (2007)), and measurements ranging from 12 to 25% were reported. Kimmoun and Branger (2007) used PIV images together with velocity measurements to estimate the void fraction in the surf zone. They reported peak values of around 0.88 near the first splashup and around 0.2 closer to the shore. More recently fiber optic sensors were used to provide more accurate estimates of void fraction. Measurements using fiber optic methods in deep water breaking waves where conducted by Rojas and Loewen (2010) and Na et al. (2018). Rojas and Loewen (2010) reported values in the range from 0.24 to 0.96. Measurements using fiber optics in waves breaking over a submerged sloping reef was conducted by Blenkinsopp and Chaplin (2007). They indicate that the peak volume of air entrained by breaking wave was approximately equal to that of the water in the splashup. They also indicate that the total energy expended in entraining air and generating the splashup was 6.5 to 14% of the total energy dissipated during breaking. As can be seen from the values of void fraction reported in the literature there is quite a wide spread in measured void fraction. In addition to experimental measurements there have been various attempts to computationally model the complex flow processes induced by wave breaking. The most promising have been large eddy simulation (LES) studies as reported upon by Watanabe et al. (2005), Lakehal and Liovic (2011) and Ma et al. (2011), which in the latter case have made attempts to simulate the air entrainment process due to wave breaking. However, a significant limitation to validating these models remains the lack of measurement data encompassing turbulent structures in the highly dynamic region above the wave trough level.

From the above literature review it is clear that a wide range of studies have been conducted in plunging waves in the surf zone and in deep water breaking waves during the last two decades. Despite these extensive studies we found limited number of measurements of turbulence and shear stress for positions above the trough level in plunging waves in the surf zone, especially across the transition zone. We therefore endeavour in this paper to supplement existing measurements of TKE and shear stress across the outer and inner surf zones and spanning the entire water column. Further, recognizing the significant challenges in computational modeling of both hydrodynamic and sediment transport processes in the surf zone an objective is to provide data that can possibly be used for model validation. Further, recognizing that LES type models are highly computationally intensive, investigations are made into the wave phase dependent behavior of flows in different areas of the breaker zone. In particular, attention is given to whether turbulence intensities below the wave trough and near the sea bed can be represented in a wave averaged manner, as was the approach adopted by Mocke (2001) using a time independent turbulent closure model to predict measured suspended sediment concentrations and undertow profiles. Such models present the possibility of simulating sediment transport and mean flow processes in the surf zone in a manner more suited to implementation in coastal engineering practice.

It will be beneficial at this point to review the basic equations describing the hydrodynamics in the surf zone. The position and velocity of a fluid element will be denoted, using cartesian tensors, as x_i and u_i, $i = 1, 2, 3$. Where $x = x_1$ and $y = x_2$ are the positions in the horizontal directions parallel and perpendicular, respectively, to the wave propagation, and $z = x_3$ is the position in the vertical direction. The corresponding velocities are $u = u_1$, $v = u_2$ and $w = u_3$, respectively. It is customary to decompose the instantaneous velocities in the surf zone as $u_i = \langle u_i \rangle + u'_i = U_i + \tilde{u}_i + u'_i$, where $\langle u_i \rangle$, U_i, $\tilde{u}_i$ and u'_i are the velocity components due to phase-ensemble averaging, time averaging, wave orbital contribution and the turbulent fluctuating part, respectively. Note that $\langle u_i \rangle$, U_i, $\tilde{u}_i$ and u'_i will be functions of position x_i and all, excepting U_i, will be functions of time as well. Substituting the above decomposition into the Navier–Stokes equation and performing phase-ensemble averaging we obtain

$$\frac{\partial \langle u_i \rangle}{\partial t} + \frac{\partial \langle u_i \rangle \langle u_j \rangle}{\partial x_j} = \frac{1}{\rho} \frac{\partial}{\partial x_j} \left(-\langle p \rangle \delta_{ij} + 2\mu_{ij} \left(\frac{\partial \langle u_i \rangle}{\partial x_j} + \frac{\partial \langle u_j \rangle}{\partial x_i} \right) - \rho \langle u'_i u'_j \rangle \right) \tag{1}$$

In the above ρ and μ are the fluid density and the dynamic viscosity, respectively and p is the dynamic pressure. Time averaging the above and also using the continuity equation gives the equation describing the mean flow to be

$$\frac{\partial}{\partial x_j} \left(U_i U_j + \overline{\langle \tilde{u}_i \tilde{u}_j \rangle} + \overline{\langle u'_i u'_j \rangle} \right) = \frac{1}{\rho} \left(-\frac{\partial P}{\partial x_j} \delta_{ij} + \mu \frac{\partial^2 U_i}{\partial x_i x_j} \right) \tag{2}$$

The terms $\overline{\langle \tilde{u}_i \tilde{u}_j \rangle}$ and $\overline{\langle u'_i u'_j \rangle}$ multiplied by ρ are the wave and turbulence Reynolds shear stresses, respectively.

The behavior of the turbulent kinetic energy (TKE), which is defined as $k = \frac{1}{2} \langle u'_i u'_j \rangle$, is described by the following equation

$$\frac{\partial k}{\partial t} + \frac{\partial \langle u_j \rangle k}{\partial t} = -\frac{\partial}{\partial x_j} \left(\frac{1}{\rho} \langle u'_j p' \rangle + \langle u'_j k' \rangle - 2\nu \langle u'_j s'_{ij} \rangle \right) - \langle u'_i u'_j \rangle S_{ij} - 2\nu \langle s'_{ij} s'_{ij} \rangle \tag{3}$$

where $k' = \frac{1}{2} u'_i u'_j$, and S_{ij} and s'_{ij} are the strain rates due to the phase-ensemble averaged flow and turbulence, respectively. The above equation indicates that the local time rate of change of TKE is due to convection by the mean flow (2nd term on the left), by diffusive transport by pressure, turbulence fluctuations, transport by viscous stress (terms in brackets on the right) and by the production and dissipation terms (last two terms on the right).

The present paper provides details of an experimental study of a strong plunging wave breaking on 1:20 slope beach. Fluid velocities were measured using particle and bubble imaging techniques. The instantaneous velocity flow fields were then processed using phase-ensemble averaging and time-averaging to extract wave orbital velocities, wave shear stresses, turbulence intensities, turbulent kinetic energies and Reynold stresses. Measurements are conducted throughout the outer and inner surf zones and over the entire water column. In Section 2 the experimental setup and data acquisition is discussed. Section 3 provides details of the results, including general features of mean water levels, wave heights and velocity flow fields, and evolution of the mean velocities and turbulence intensities, turbulent kinetic energies (TKE) and shear stresses across the outer and inner surf zones. The summary and conclusion are provided in Section 4.

2. Experimental setup and procedures

The experiments were conducted in a glass walled flume. The flume is 20 m long, 0.75 m wide and 0.8 m high. This research is an extension of work previously published by Govender et al. (2002) and the present experimental work was conducted in the same glass walled wave flume but with the following changes; The wave generator has been replaced with a Wallingford piston type generator and the arrangement of the bottom profile has been reconstructed. The bottom profile is a 1:20 slope cemented beach. The schematic of the flume and bottom profile is shown in Fig. 1.

The still water depth on the flat section of the flume was 61.8 cm and plunging waves having period of 2.5 s and a wave height of 12 cm in the flat section of the flume was used. Water level across the flume was measured using a set of capacitive wave gauges. The break point was approximately 4 m from the still water mark on the beach and the wave height at the breakpoint was 21.5 cm. The mean and still water depths at the break point was 19.6 cm and 20.0 cm, respectively. This wave broke quite violently entraining large quantities of air and generating large scale coherent eddies that move downwards and seawards.

The fluid velocity in the wave was measured over a region beginning just after the break point and extending approximately 3 m shorewards. The flowfields were measured at six sections spanning the outer and the inner surf zones. Each of the sections are approximately 30 cm wide and are labeled as sections S1 to S6 in Fig. 1 and the center positions of these sections will be referred to as P1 to P6, respectively. The fluid velocity spanning the entire water column and including the highly aerated crest region was measured using the same video technique as mentioned in the previous publications (Govender et al., 2002), which we also describe in greater detail below. This technique was used to report on the earliest measurements of fluid velocities in the crest and roller region of spilling and plunging waves. Other researchers have subsequently applied a similar approach and referred to it as bubble image velocimetry (Ryu et al. (2005), Na et al. (2016, 2018)).

Our primary focus in all our previous work has been to obtain velocity estimates in the roller and crest region of a breaking wave, while at the same time still obtaining measurements below the trough level. We continue in the present work to expand and provide a more comprehensive study of the plunging wave case. The technique we use involves tracking the motion of neutrally buoyant polystyrene particles as well as air bubbles created as a result of wave breaking. We have found previously that the motion of air bubbles in breaking waves and turbulent flows tend to be 'locked' withing the flowing fluid and tend to move with the same velocity as the surrounding fluid.

The setup used to track bubble motion and the neutrally buoyant particles is shown in Fig. 2. A light box, containing two banks of stroboscopes and a length-wise slit at the bottom, is capable of producing a double pulsed sheet of light when triggered. The light box is placed above the flume as shown, close to the flume wall but away from the

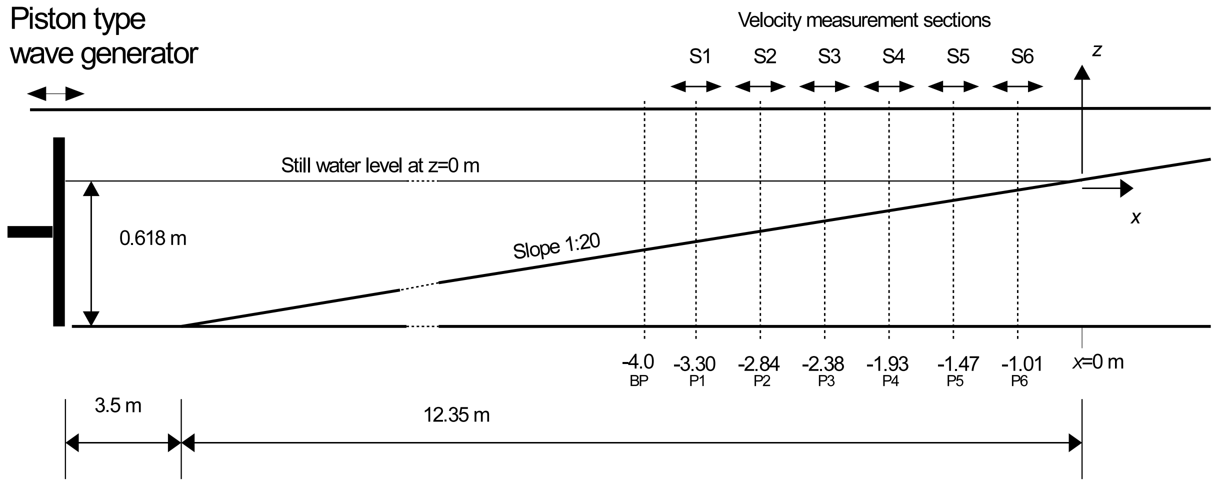

Fig. 1. Schematic of the wave flume and velocity measurement sections/stations. The center position of each section is labeled P1 to P6.

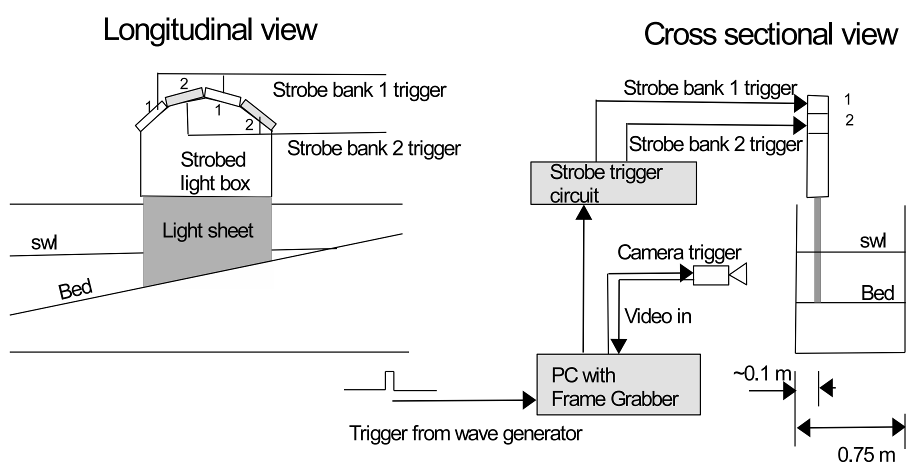

Fig. 2. Experimental setup for imaging bubbles and neutrally buoyant particles.

side wall boundary layer. The bubble and seeded flow is imaged using a progressive CCD camera connected to a video capture card in a PC. The light box is moved back and forth in the transverse direction to the flume (in the y direction) until a sharp crisp image of the bubbles is visible while at the same time ensuring to be away from the side wall boundary layer. A trigger signal from the wave generator allows us to capture images at a particular wave phase. When triggered, the camera is setup to capture two consecutive images of the flow at the usual TV frame rate of 60 Hz. At the same time the strobe bank 1 is setup to pulse the light sheet near the end of the exposure time of the first frame and strobe bank 2 is setup to pulse the light sheet towards the beginning of the exposure time for the second frame. The time between strobing of bank 1 and bank 2 is the sampling time ΔT. The entire measurement section was darkened by covering with black plastic sheeting.

Once we have two images of the flow separated by a time ΔT, we estimate the instantaneous velocity field as follows: consider a point (i, j) (in units of pixels) in the first image and a sub-image of size 32 by 32 pixel centered at (i, j). We cross-correlate this sub-image with the corresponding sub-image in the second frame. The position of the peak in the 2D cross correlation gives a measure of the displacement of the particles during the sampling time. Dividing by the sampling time and then converting to real units gives the instantaneous velocity at the point (i, j). We repeat the above process at points in the image spaced 16 pixels vertically and horizontally. Our pixel to cm conversion was in the range from 20 pixels/cm to 29 pixels/cm, depending on the measurement position and the size of area being imaged. Thus we obtained velocity estimates spaced 0.75 cm (or less) vertically and horizontally and each velocity estimate is an average over the sub-image and corresponds to a fluid area of 1.5 by 1.5 cm (or less). It is important to note that we have adopted not to use a laser light in our measurements. Laser light will not work in the aerated crest and roller area due to speckle formation which does not maintain its features as the bubbles move. Thus rendering cross correlation useless in this case. Further in strong plunging waves aeration and bubbles structures penetrate deep down in the water column reaching the bed level and extend into the trough region, thus preventing laser measurements even below the trough level. Measurements in these cases involving lasers exclude measurements in the intense bubble areas.

The camera in our setup is capable of imaging a 25 cm length-wise section of the flume, while still maintaining sufficient spatial resolution. To build up the velocity flow field over the entire wave we capture image-pairs at twenty equally spaced phases of the wave. For a particular wave phase setting, we capture 100 image pairs using a sampling time of 1.8 ms and another 100 image pairs using sampling time of 0.8 ms. The longer sampling time ensures that the very small velocities are not missed and the shorter sampling time ensures that the very high velocity in the crest are captured. In the crests of the wave very high velocities are observed and only the 0.8 ms sampling time contributes to valid velocity estimate. Thus at each bin position (i, j) in the image we have in excess of 100 data points for positions below the trough level and approximately 80 to 100 data points in the crest region. This we found to be adequate to ensure convergence of

Table 1
Calculation of uncertainty δv in velocity, for various pixel displacement, and using a sampling time of $\Delta T = 0.8$ ms, and uncertainty in pixel position of $\delta x = 0.125$ pixels. Δx is the displacement of the fluid element corresponding the pixel displacement. A pixel to cm calibration of 20 pixels/cm is used.

Pixel displacement	Δx (cm)	v(cm/s)	δv (cm/s)	% error
0.5	0.025	31.3	7.8	25
1	0.05	62.5	7.9	13
3	0.15	188	8.2	5
5	0.25	313	8.7	4

Table 2
Calculation of uncertainty δv in velocity, for various pixel displacement, and using a sampling time of $\delta T = 1.8$ ms, and uncertainty in pixel position of $\delta x = 0.125$ pixels. Δx is the displacement of the fluid element corresponding to the pixel displacement. A pixel to cm calibration of 20 pixels/cm is used.

Pixel displacement	Δx (cm)	v(cm/s)	δv (cm/s)	% error
0.5	0.025	13.9	3.4	25
1	0.05	27.8	3.5	13
3	0.15	83.3	3.5	4
5	0.25	139	3.6	3

the mean and turbulence velocities. We found that mean velocities tend to converge after approximately 30 measurements and the turbulence velocities tend to converge after approximately 50 measurement points.

At each phase setting the 200 image pairs are processed to yield 200 instantaneous flow fields. These instantaneous flow fields are phase-averaged to yield the phase-averaged horizontal and vertical velocities. At each bin position (i,j) the phase averaged velocities $\langle u(i,j)\rangle$ and $\langle w(i,j)\rangle$ are calculated using

$$\langle u_p(i,j)\rangle = \frac{1}{N_{bin}}\sum_{n}^{N_{bin}} u_{p,n}(i,i), \qquad \langle w_p(i,j)\rangle = \frac{1}{N_{bin}}\sum_{n}^{N_{bin}} w_{p,n}(i,j) \tag{4}$$

where N_{bin} is the number of samples available at each bin position and the subscript n refers to individual samples in each bin and p refers to the phase. The instantaneous turbulence velocities $\langle u'\rangle$ and $\langle w'\rangle$ are calculated using,

$$u'_{p,n}(i,j) = u_{p,n}(i,j) - \langle u_p(i,j)\rangle$$

$$w'_{p,n}(i,j) = w_{p,n}(i,j) - \langle w_p(i,j)\rangle$$

The phase averaged values $\langle u_p'^2\rangle$, $\langle w_p'^2\rangle$, $\langle (u'w')_p\rangle$ etc. are then calculated using equations similar to Eq. (4).

The phase averaged TKE is estimated using

$$\langle k_p(i,j)\rangle = \frac{1.33}{2}\left(\langle u_p'^2(i,j)\rangle + \langle w_p'^2(i,j)\rangle\right)$$

2.1. Uncertainties in velocity measurements

In estimating the velocity of a fluid element contained with the sub images of size 32 × 32, the cross correlation results were interpolated by a factor 8, thus enabling position of the peak to be estimated with sub-pixel resolution of 0.125 pixel. If Δx is the displacement of a fluid element withing the sub image in a sampling time ΔT then the velocity is given by $v = \Delta x/\Delta T$, and the uncertainty in the velocity, from statistical analysis, is given by

$$\delta v = \left|\frac{\Delta x}{\Delta T}\right|\sqrt{\left(\frac{\delta x}{\Delta x}\right)^2 + \left(\frac{\delta t}{\Delta T}\right)^2}$$

where δx and δt are the uncertainties in the position of the correlation peak and sampling time, respectively. The uncertainty in the sampling time is approximately 0.02 ms and is due to the finite duration of the strobed light. Tables 1 and 2 shows the uncertainty in velocities calculated using a pixel to cm conversion of 19 pixels/cm, uncertainty of 0.125 in pixel position and uncertainty in sampling time of $\delta T = 0.02$ ms. Table 1 corresponds to a sampling time of 0.8 ms, and Table 2 corresponds to a sampling time of 1.8 ms.

From the above we see that typical uncertainty in velocities is approximately 13% or less for pixel displacements of one pixel or greater. The very small displacements of 0.5 pixel has an error of approximately 25%. To minimize the error in these small displacements, as mentioned previously, the 0.8 ms sampling time is used to capture the high velocities, while the 1.8 ms sampling time is used to capture the smaller velocities.

Table 3
Position of breakpoint BP and mid points P1 to P6 (x), still water depth (d), mean water depth (h) and wave heights (H).

Position	x (cm)	d (cm)	h (cm)	H (cm)	h/h_b	H/h_b	H/h	$C=\sqrt{gh}$ (cm/s)
BP	−400	20.0	19.6	21.5	1.00	1.1	1.1	138
Mid section 1 (P1)	−330	16.5	16.6	19.4	0.846	0.99	1.17	127
Mid section 2 (P2)	−284	14.2	14.6	14.2	0.745	0.72	0.97	118
Mid section 3 (P3)	−239	12.0	12.6	11.6	0.643	0.59	0.92	108
Mid section 4 (P4)	−193	9.7	10.6	9.7	0.540	0.49	0.92	97
Mid section 5 (P5)	−147	7.4	8.7	7.9	0.444	0.40	0.91	84
Mid section 6 (P6)	−101	5.1	6.7	5.6	0.342	0.29	0.84	70

3. Results and discussion

3.1. General features of water levels, wave heights and velocity fields

In this section we provide a summary of the important characteristics of the water levels and wave heights at key positions along the surf zone. We also examine qualitatively the wave breaking process and general features of the instantaneous velocity fields at Sections 2 and 4.

As mentioned in the previous section, the wave height in the flat section of the flume near the generator was 12 cm. The wave period was set to 2.5 s and this corresponds to a deep water wavelength of 975.8 cm, calculated using $L_0 = gT^2/2\pi$. The waves reached a maximum wave height of 21.5 cm at approximately −4 m from the still water mark on the beach. This gives a surf similarity of

$$\xi_b = \frac{\tan\beta}{\sqrt{H_b/L_0}} = 0.3368$$

This put the surf similarity just outside plunging category, $0.4 < \xi_b < 2.0$, but from visual appearances and from the uniform profile of the undertow across the water column (due to higher levels of mixing) and higher levels of turbulence, the wave has the behavior of a strong plunging wave. The mean and still water depth at the breakpoint was 19.6 cm and 20.0 cm, respectively, giving H_b/h_b ratio of 1.1. These and other relevant parameters of the wave at the various measurement sections are summarized in Table 3.

The wave begins the plunge just after it reaches maximum wave height and the overturning crest then strikes the free surface in the middle of section 1. In section 2, the subsequent splashup occurs and by the time the wave gets to section 3 it is almost a fully formed bore-like breaking wave. Sections 1 to 3 then forms the outer surf zone where the transition occurs. These sections are the most dynamic part of the plunging wave. We will show later that in these sections the undertow and turbulence undergoes rapid changes in character as the wave traverses this region. Fig. 3 shows a few images of the crest plunging at section 1 and the subsequent splashup in section 2. These images show the dynamic nature of this plunging wave. Also shown in these images are the bottom bed profile, and the approximate surface profile that will be used to separate the connected body of water forming the wave from the loosely disconnected blobs of water ejected from the wave. Fig. 4 show six images of consecutive phases at section 2, beginning with the approach of the crest and splashup followed by images of the waves as it passes. Note, because of the manner in which

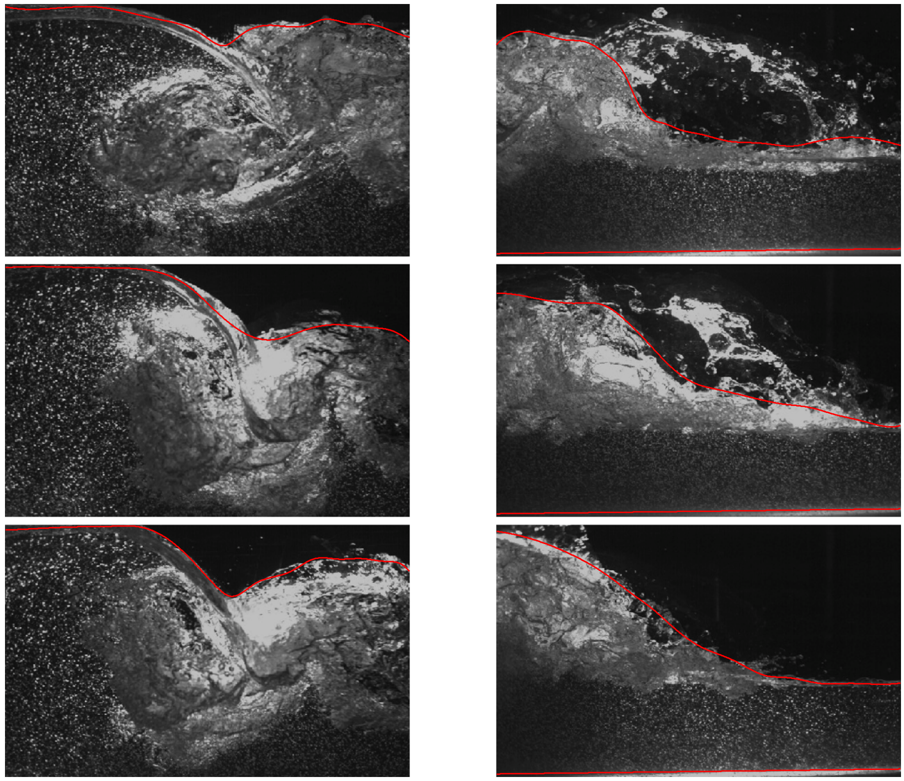

Fig. 3. Three images of the crests appearing in (left column) section 1 and (right column) section 2.

we acquire the images, these are images taken from different wave cycles. Panel (a) shows the crest and splashup reaching section 2. Panel (b) corresponds to a time 0.125 s later and shows the peak of the crest. Clearly evident from the bubble structures in this image are two large vortices, one near the front face and another towards the left bottom of the image. One can just about make out the trapped air or water surrounded by a region of aerated water towards the lower left of this image. In panel (c) the wave has moved further and the large eddies made visible by the air bubbles is still discernible. Also evident from panels (b) and (c) is the penetration of the aeration into the lower part of the wave. The images in panels (d) to (f) are of the troughs moving past. In these images one can see the deep penetration of the air bubbles reaching the bed in all three of the images. In the image in panel (f) it is possible to see an eddy still existing near the bottom right, made visible by the air bubbles.

Fig. 5 shows the instantaneous velocity fields corresponding to the images in Fig. 4. There are certain features worth noting. Firstly the high resolution plot of the vectors is clearly evident. Also there are a few missing vectors at certain points or bin positions in each plot. These missing vectors are due to a poor correlation of structure between the sub-images centered at that point. These missing vectors are not interpolated but are filled in via phase ensemble averaging. Thus all the data presented in this paper are from actual measurements and not extrapolated or interpolated. A close examination of the vectors in these plots reveal extensive amount of information on the eddy structure, some of which were made visible by the presence of the air bubble. But there are other features not so easily seen in the images. The large scale eddies seen in the images show up quite clearly in the vector fields. But in addition there are other smaller eddies visible in these plots as well. One can pick out at least two eddies in each plot. The larger eddies tend to be elongated in the horizontal direction, due possibly to the limited water depth and the magnitude of the mean velocities. Panel (f) shows a large eddy at the bottom right of approximately 10–15 cm in dimension horizontally. This is of the order of the water depth and wave height at this position. Examining the images and velocity flowfields, similar to those in Figs. 4 and 5, at section 4, we see much more eddies structures, consisting of large scale vortices as well as smaller scale vortices. The large scale vortices are also of the order of the water depth.

3.2. Time-averaged velocities and velocity fluxes

Fig. 6 displays the time-averaged velocity vectors spanning the region from −350cm to −95cm from still water mark on beach. While we measure the velocity flow field at each section at approximately every 0.75 cm vertically and horizontally, for the purposes of displaying and analysis we display data corresponding to the middle of each section and 10 cm on either side. Thus from each section we display three vertical strip of vectors. The middle column of vectors, in each group of three, corresponds to the center of sections S1 to S6, i.e. at positions P1 to P6. The figure clearly displays velocity measurement spanning the entire water column, from 1 cm above the bed to 1–2 cm below the wave crest level. There is a net offshore flow due to the undertow current and a net onshore flow due mostly to the transport associated with the wave roller. The undertow plays a significant role in transporting suspended sediments offshore.

Before examining the details of the structure of the velocity profiles, it might be instructive to examine the onshore and offshore mass fluxes. The present experiment involves a closed system and therefore, by conservation of mass, the net mass flow across any transverse cross-section of the flume must be zero. The mass flux due to the undertow can be computed using

$$M_{offshore} = \sum \rho_{water} u_i dz = \rho_{water} \sum u_i dz$$

and the onshore flux is

$$M_{onshore} = \sum \rho_{crest} u_i dz = \rho_{avg,crest} \sum u_i dz$$

where the sum runs over all negative velocity for the offshore flux and over all positive velocity for the onshore flux and dz is the spatial separation of the velocity measurements. The sum $\sum u_i dz$ without the density represents the velocity flux. Fig. 7 shows the computation

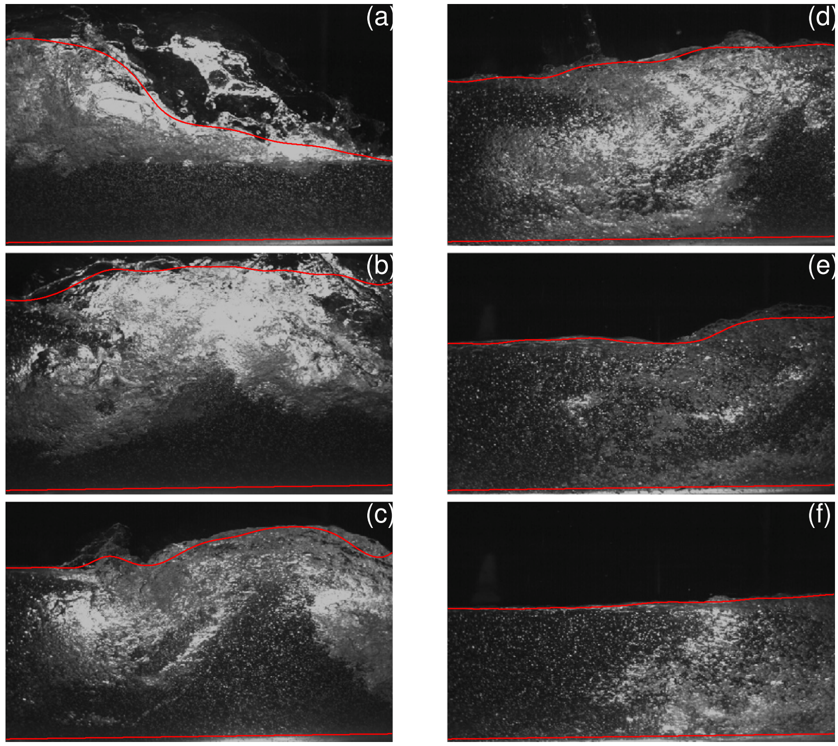

Fig. 4. Images at six consecutive phase positions (from top to bottom and left to right) showing approaching crest followed by phases in the trough at section 2. Note these images are taken from different wave cycles.

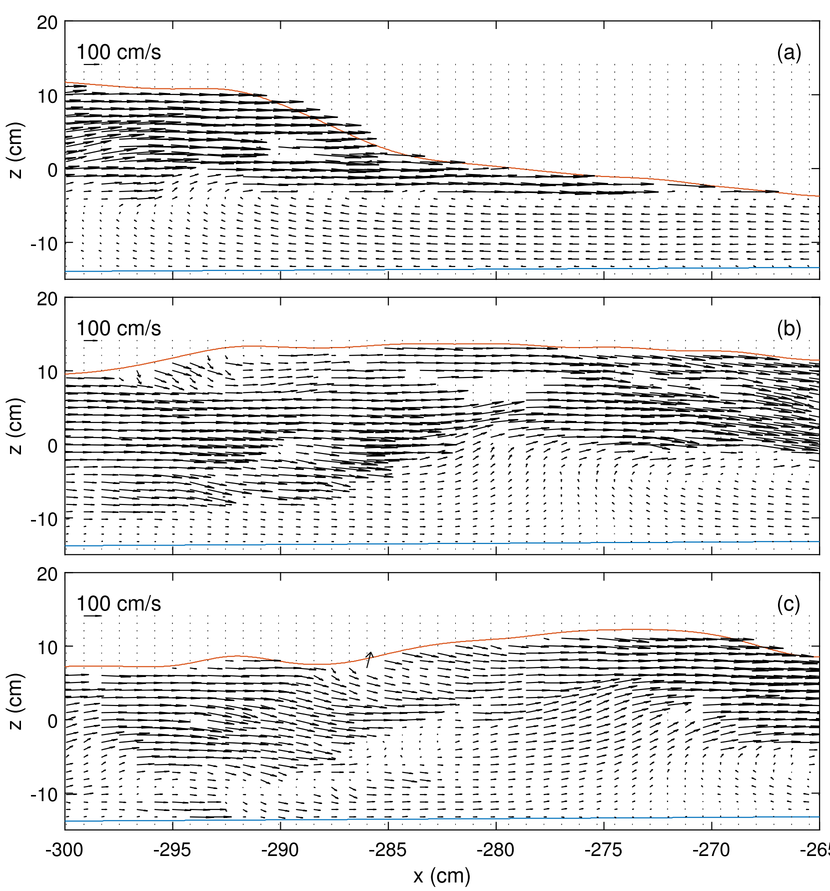

Fig. 5(a–c). Instantaneous velocity fields at section 2 corresponding the images in panels (a) to (c) in Fig. 4.

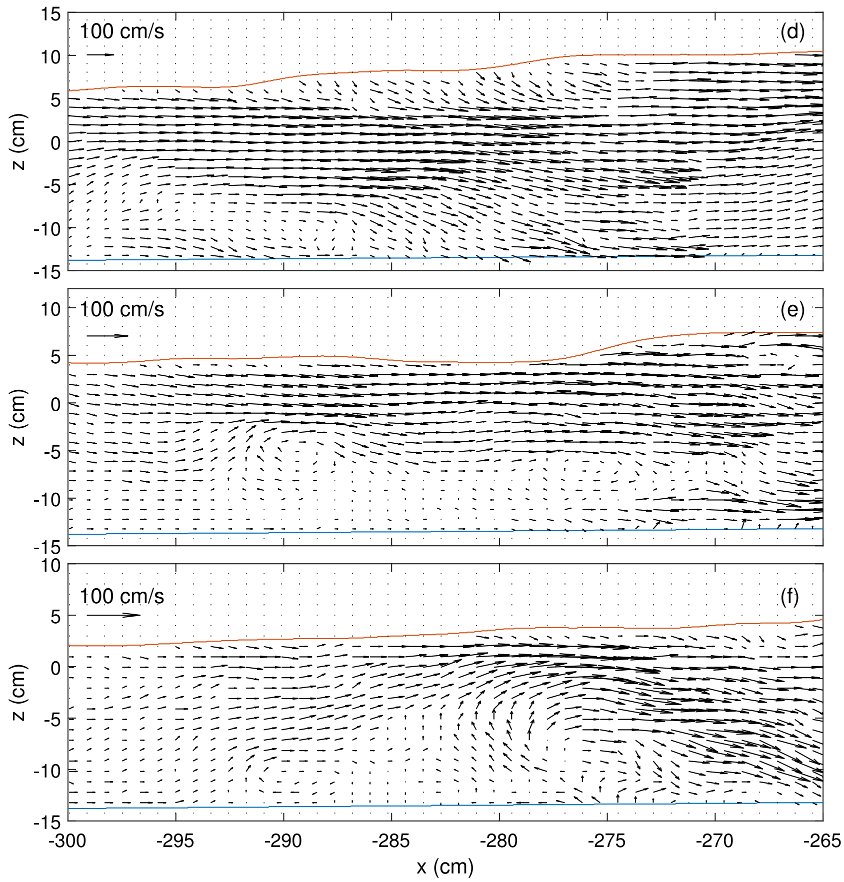

Fig. 5(d–f). Instantaneous velocity fields at section 2 corresponding the images in panels (d) to (f) in Fig. 4.

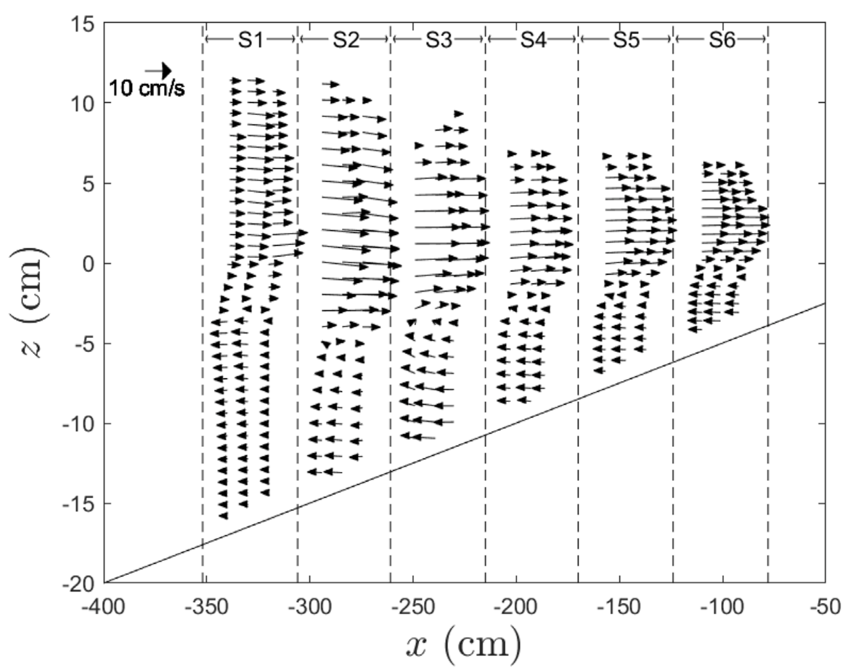

Fig. 6. Time-averaged velocity vectors across the water column at three horizontal positions, spaced 10 cm apart at each of the measurement sections S1 to S6. The center vertical strip of vectors at each measurement section correspond to the vectors at the positions labeled P1 to P6 in Fig. 1.

of the onshore and offshore velocity fluxes. At or near the breakpoint the onshore and off shore fluxes are almost equal and this is expected since there is minimum aeration and the roller is non-existent at this point. However, the profiles of these changes as one moves across the surf zone. The onshore velocity flux (stars) shows an initial increase, reaching a peak around $x = -270$ cm (in section S2) and an almost linear decrease thereafter. Over the same horizontal section the velocity flux due to the undertow (crosses) has a different character

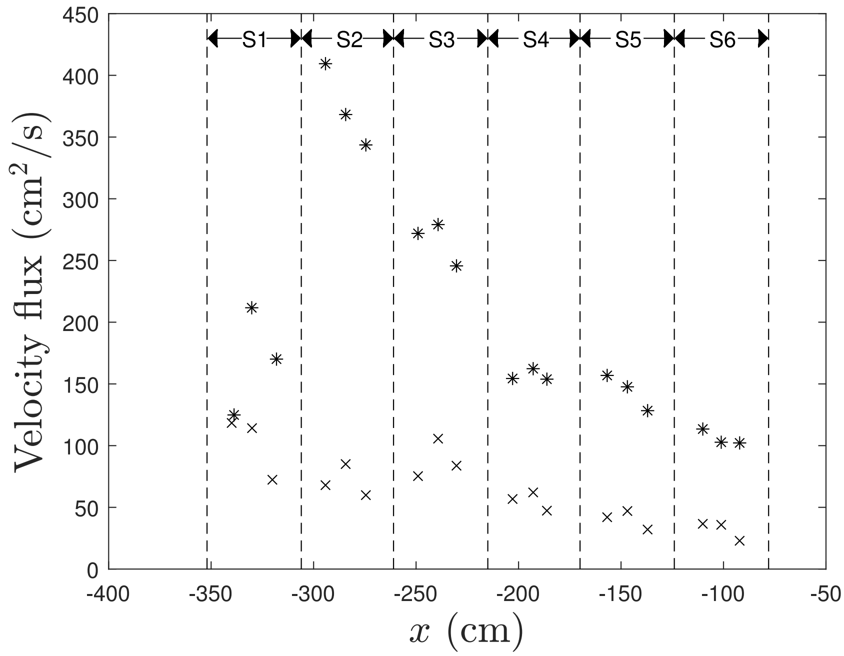

Fig. 7. The onshore (*) and off shore (x) velocity fluxes across the outer and inner surf zones.

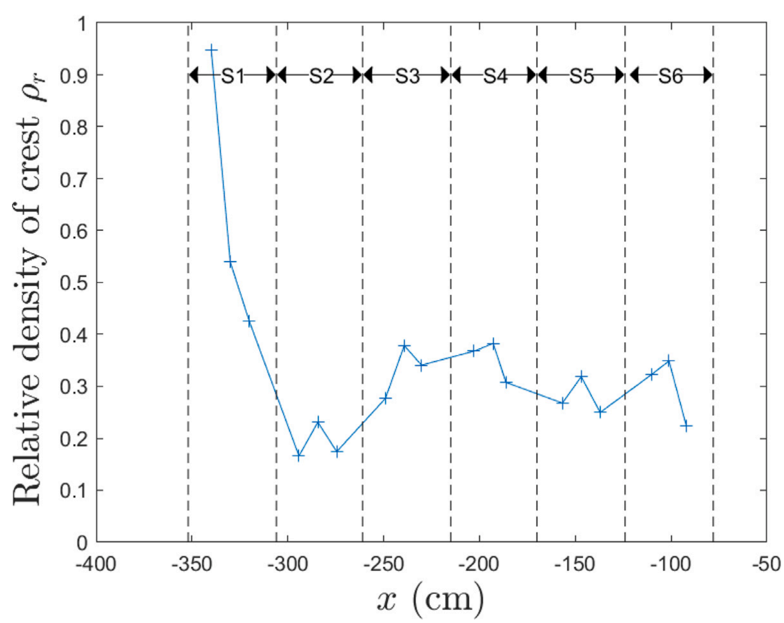

Fig. 8. Average relative density above trough level across the outer and inner surf zones.

and begins to decrease, reaching a minimum around the position where the forward flux reaches its maximum (in section S2). The offshore flux then increases reaching a maximum in section S3, then decreasing almost linearly thereafter. The region spanned by sections S1 to S3 is a dynamical transition region were the plunging jet penetrates into the lower part of wave as it moves forward and where subsequent splashup and the full formation of the roller takes place. This region roughly represents the outer surf zone. It is an area that traditionally has been very difficult to investigate using traditional techniques, such as LDA or hotwire anemometry and even techniques such as PIV have not been successful due to the high aeration content in this region. Although a fair amount of studies have been conducted over the last two decades, the outer surf zone is probably the least understood section of the surf zone and it is definitely worthy of more investigation to corroborate and supplement existing data.

Since the net onshore mass flux must equal the net offshore mass flux, we can use this to estimate an average relative density of the fluid in the crest and roller area using

$$\rho_r = \frac{\rho_{avg,crestandroller}}{\rho_{water}} = \frac{\sum_{undertow} u_i dz}{\sum_{above} u_i dz}$$

and Fig. 8 shows the variation of the relative density across the outer and inner surf zones. The dip in the relative density in the crest across the outer surf zone is clearly evident. In the inner surf zone the relative density varies from 0.2 to 0.4. However, as pointed out previously, there is aeration present below the trough level and therefore the ratio of the forward and offshore mass fluxes gives the density of the crest relative to that of the fluid below trough level. However, the level of aeration is not as high as that in the crest and therefore as a first approximation our calculation gives an upper bound for the density

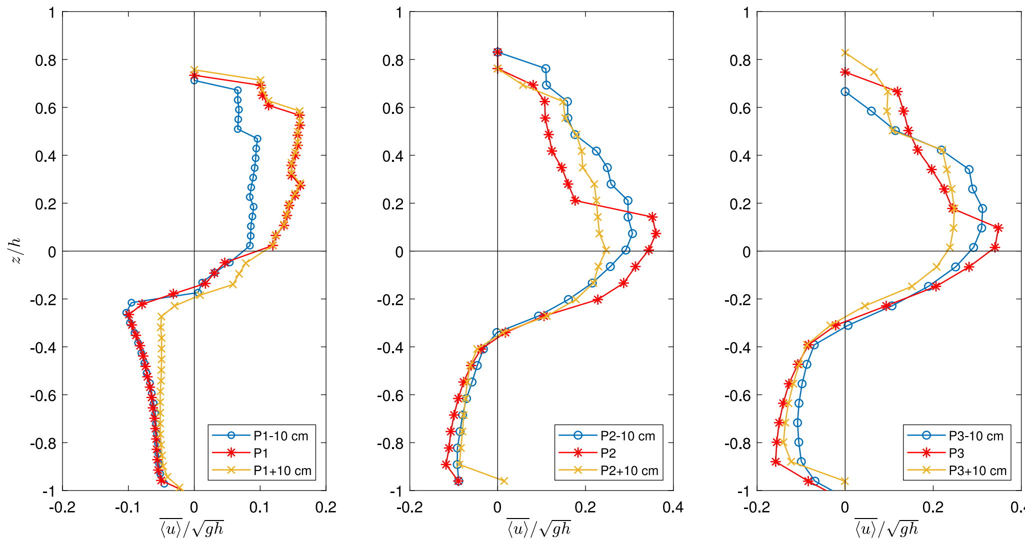

Fig. 9. Time-averaged horizontal velocity as a function of depth at Section S1 to S3. The star (*) represents measurements at the center of each section, and the circles (o) and crosses (x) are measurements 10 cm to the left and right of the center, respectively.

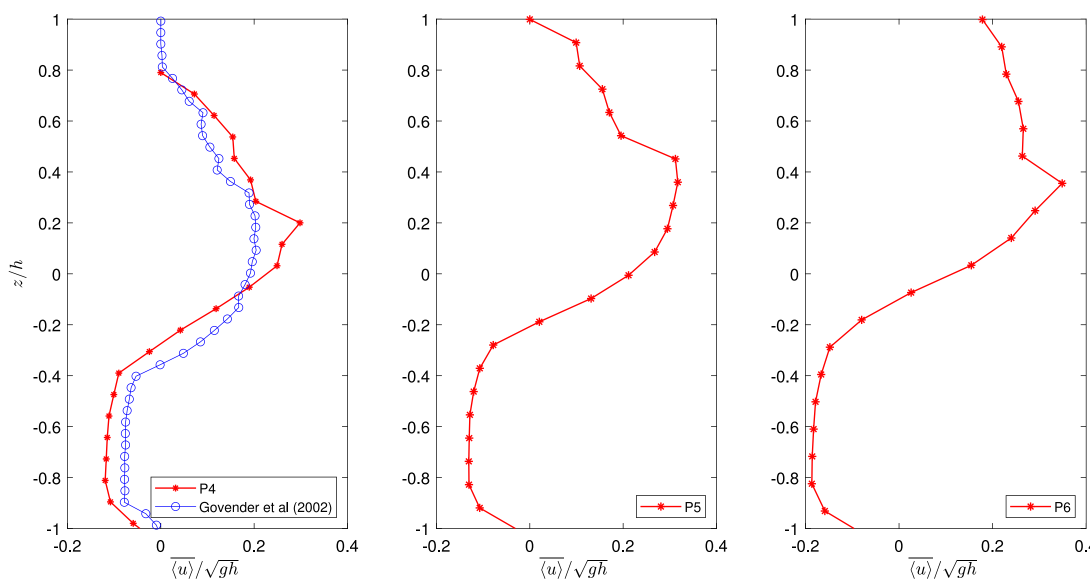

Fig. 10. Time-averaged horizontal velocity as a function of depth at mid position P4 (h/h_b=0.540), P5 (h/h_b=0.444) and P6 (h/h_b=0.342). Also shown are the undertow measurements by Govender et al. (2002) at a position h/h_b=0.538.

in the crest relative to water. These numbers would indicate an even higher level of aeration in the roller and will greatly influence the actual turbulent kinetic energy content and the fluid flow properties above the trough level.

Returning to the detail structure of the undertow profile, Figs. 9 and 10 shows the vertical profile of $\overline{\langle u \rangle}/\sqrt{gh}$ in sections S1 to S6 normalized with respect to the local mean water depth. At Section 1 the profile initially (at the middle and 10 cm seawards) resembles that of prebreaking waves. The velocity increases in the negative direction from the bed upwards and just around the trough level the velocity begins to change direction and point shorewards. Still within section 1 but to the right of the middle, the profile begins to transform, becoming approximately uniform across the depth below the trough level. The middle of this section is were the overturning crest plunges into the trough in front.

The transformation of the undertow profile continues into Section 2, the magnitude now decreasing from the bed upwards. The point at which the velocity changes sign is pushed further down the water column resulting in a low offshore velocity flux, as we have seen already. From here onwards the undertow profile is almost uniform across the depth which is typical of plunging waves. Also shown in Fig. 10 are the measurements of the undertow by Govender et al. (2002) for a position similar to that of position P4. The normalized undertow at P4 in the present experiment compares very well with the previous test case of Govender et al. (2002) at a similar position.

3.3. Phase-averaged velocities and wave shear stress

The phase-averaged velocity flow fields as a function of time, at the center positions P1 to P6 of each measurement section, are shown in Figs. 11 to 13. These figures are generated by extracting as follows: from each of the twenty phase ensembled flow fields (which are flow fields measured as a function of horizontal distance), a vertical column of vectors corresponding to the center of the section are extracted and stacked side by side creating a time stack. Note the flowfields are plotted as a function of $-t/T$ so that the flowfields and surface

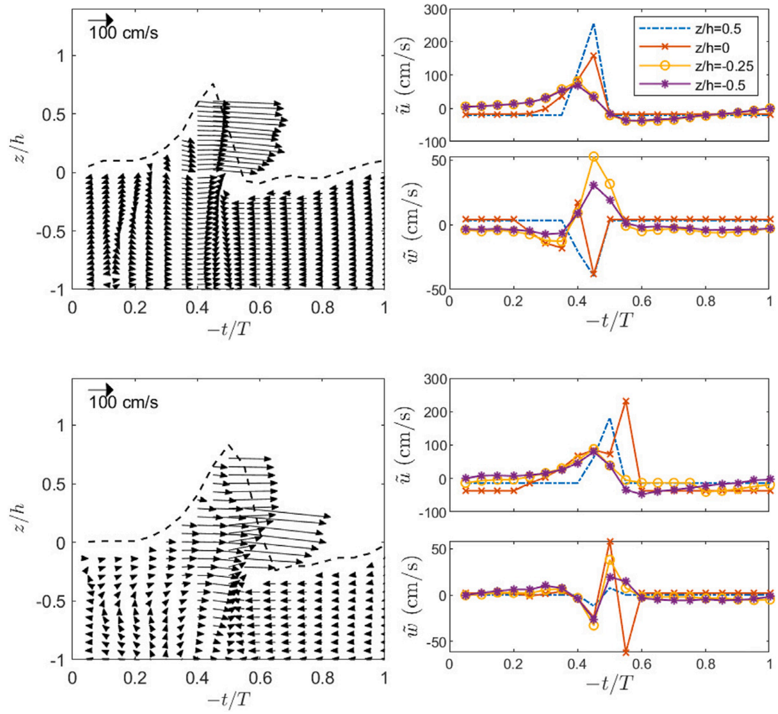

Fig. 11. Phase-averaged velocity flowfields as function of $-t/T$ at center positions (top left) P1 and (bottom left) P2. Plots of the orbital velocities at z/h equal to (dashed line) 0.5, (crosses) 0, (circles) −0.25 and (stars) −0.5 are shown on the right for each section.

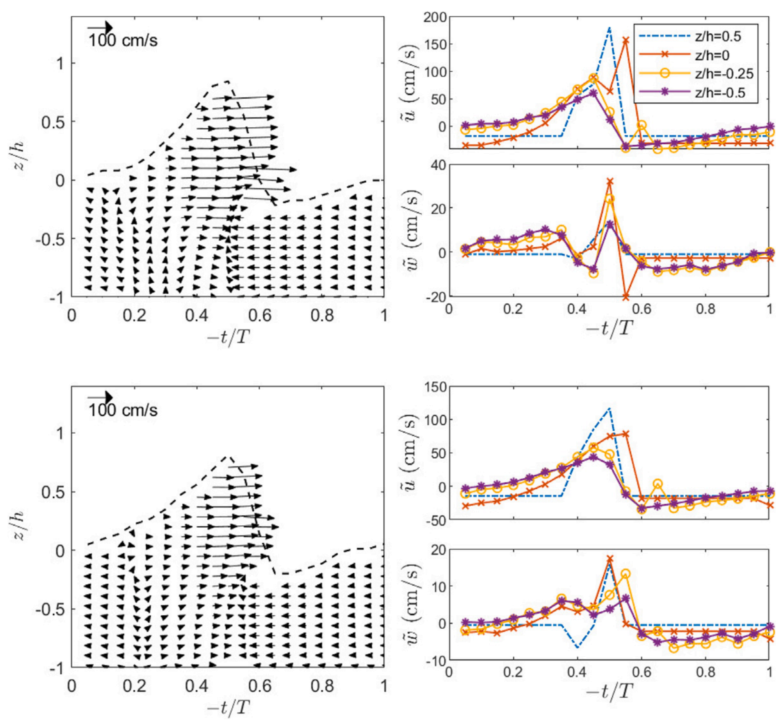

Fig. 12. Phase-averaged velocity flowfields as function of $-t/T$ at center positions (top left) P3 and (bottom left) P4. Plots of the orbital velocities at z/h equal to (dashed line) 0.5, (crosses) 0, (circles) −0.25 and (stars) −0.5 are shown on the right for each section.

profile appears as one would observe the actual wave passing from left to right. Also shown in these plots are the approximate wave profiles generated by tracking the highest vector in each column. The plots are also presented so that the peak of the wave appears at $-t/T = 0.5$.

These plots highlight the evolution of the wave as it progresses into the surf zone. The wave profile changes from cnoidal near the breakpoint to sawtooth in the inner surf zone. The velocity streamlines also show significant changes in pattern. The stream lines are more symmetrical about the wave crest at the breakpoint and becoming asymmetrical as the wave breaking continues in the surf zone. Peak values of velocity occur in the wave crests, while velocities in the troughs are very much smaller in magnitude. A scale vector is provided in each plot to assist in judging the relative magnitude of velocities.

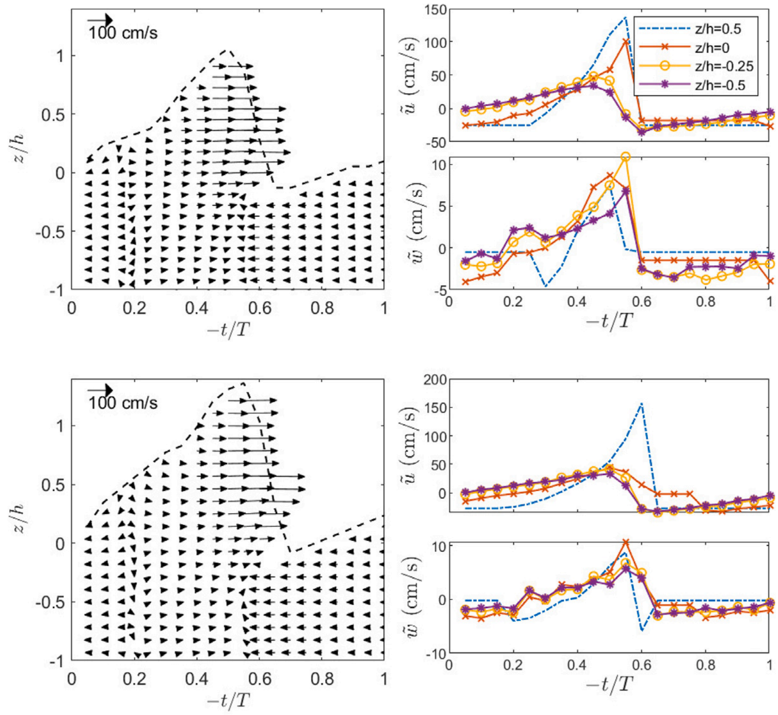

Fig. 13. Phase-averaged velocity flowfields as function of $-t/T$ at center positions (top left) P5 and (bottom left) P6. Plots of the orbital velocities at z/h equal to (dashed line) 0.5, (crosses) 0, (circles) −0.25 and (stars) −0.5 are shown on the right for each section.

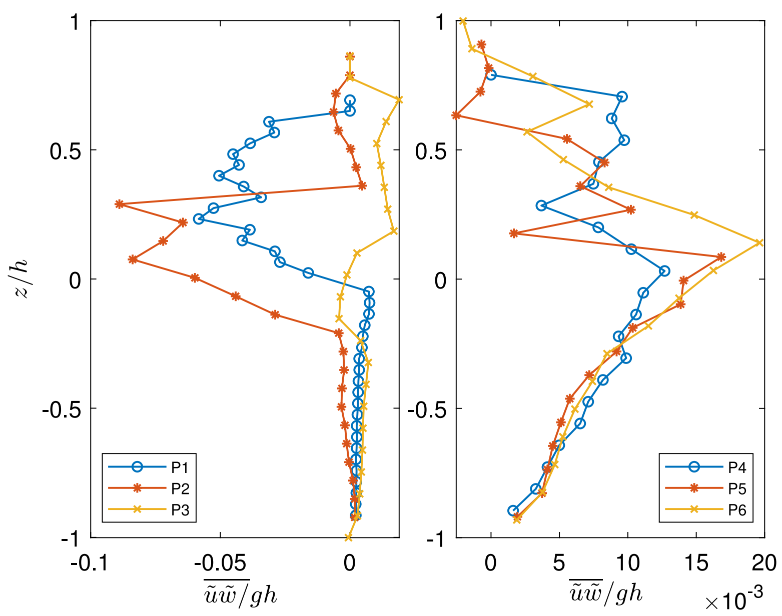

Fig. 14. Time-averaged wave shear stress $\overline{\tilde{u}\tilde{w}}$ as a function of z/h at the center position of each section.

Along side each flowfield, the plots of the wave orbital velocities $\tilde{u}$ and $\tilde{w}$ at various depths are also shown. These plots give further insight into the evolution of the velocities. The horizontal component $\tilde{u}$ has a shape resembling that of the surface profile at all stations, while the vertical component undergoes significant changes. Near the breakpoint at positions P1 to P3, $\tilde{u}$ and $\tilde{w}$ have an approximate phase difference of 45 degrees for positions below the trough level, but this changes as we move to higher vertical positions, $\tilde{u}$ and $\tilde{w}$ tending to be 180 degrees out of phase. Further in the surf zone both $\tilde{u}$ and $\tilde{w}$ have profiles similar to the surface profile and both seems to be in phase. These changes to the phase relation between $\tilde{u}$ and $\tilde{w}$ clearly will contribute significantly to the wave shear stress.

To highlight the effects of the phase relation between $\tilde{u}$ and $\tilde{w}$, Fig. 14 shows the plots of the time average correlation $\overline{\tilde{u}\tilde{w}}$ at all center positions. This corresponds to the wave shear stress excluding $-\rho$. For positions below the trough level at P1 the correlation is practically zero, but takes on large negative values above the trough level. The large negative values above the trough level persists at station P2 and a small negative correlations begins to appear below the trough level. At station P3 the correlation starts to decrease, approaching small values across the water column. Beyond station P3 there is a reversal in the sign of the correlation becoming positive and increasing from the bottom upwards. The increase from the bottom is approximately linear, reaching a peak value around $z/h = 0$, and decreasing thereafter. We

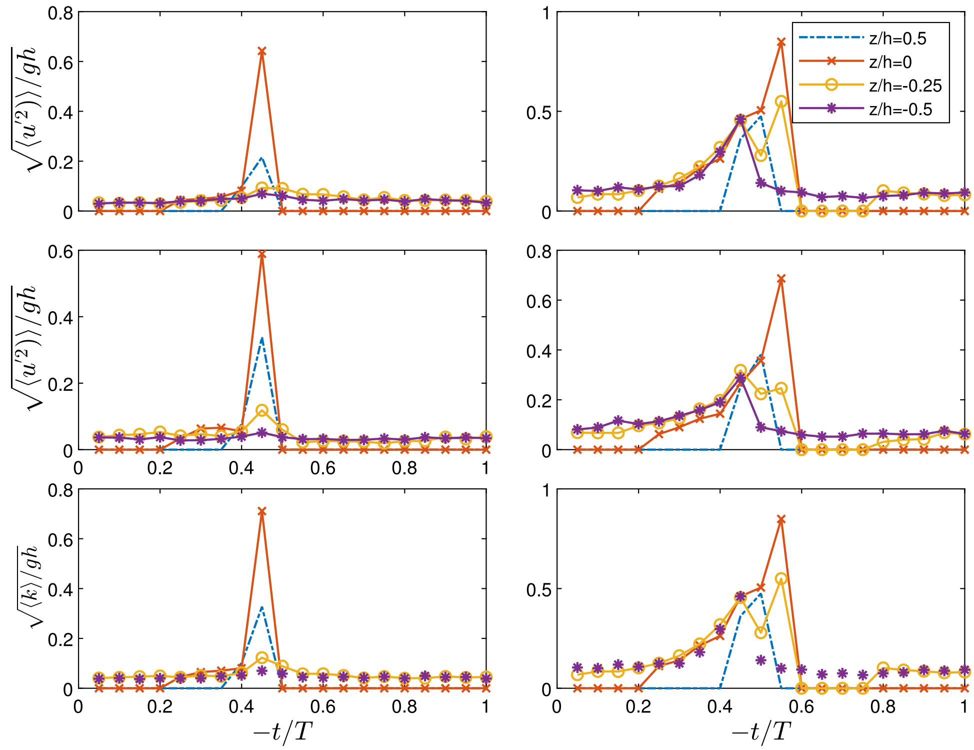

Fig. 15. Phase-averaged turbulence intensities and turbulent kinetic energy as function of $-t/T$ at center positions P1 (left column) and P2 (right column). Turbulence data for z/h equal to (dashed line) 0.5, (crosses) 0, (circles) −0.25 and (stars) −0.5 are presented.

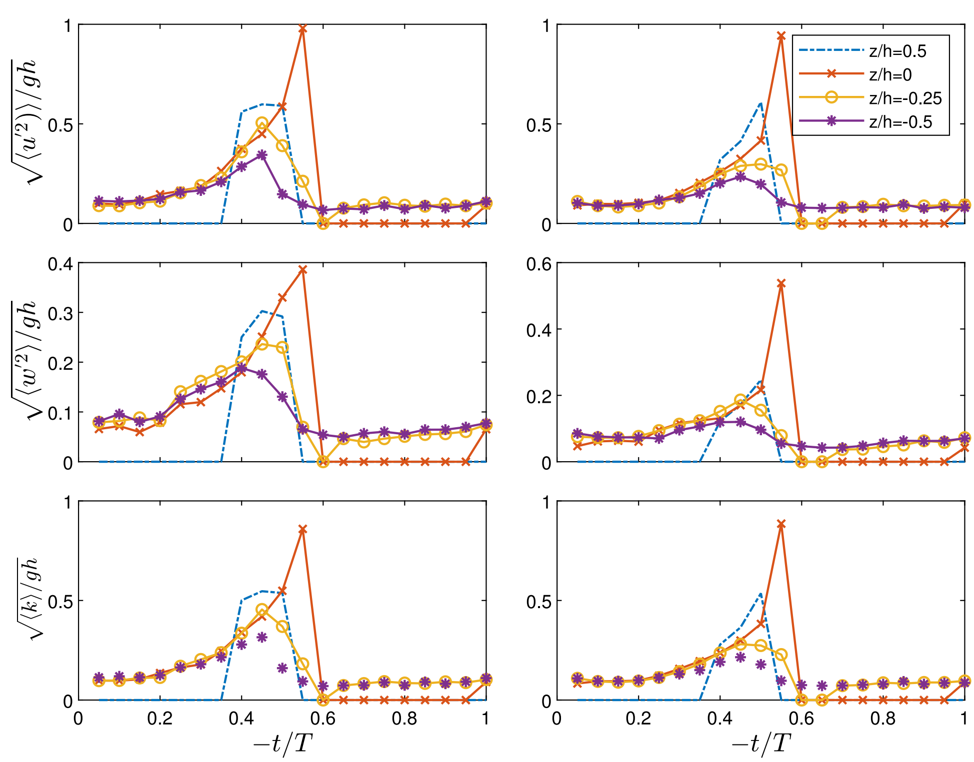

Fig. 16. Phase-averaged turbulence intensities and turbulent kinetic energy as function of $-t/T$ at center positions P3 (left column) and P4 (right column). Turbulence data for z/h equal to (dashed line) 0.5, (crosses) 0, (circles) −0.25 and (stars) −0.5 are presented.

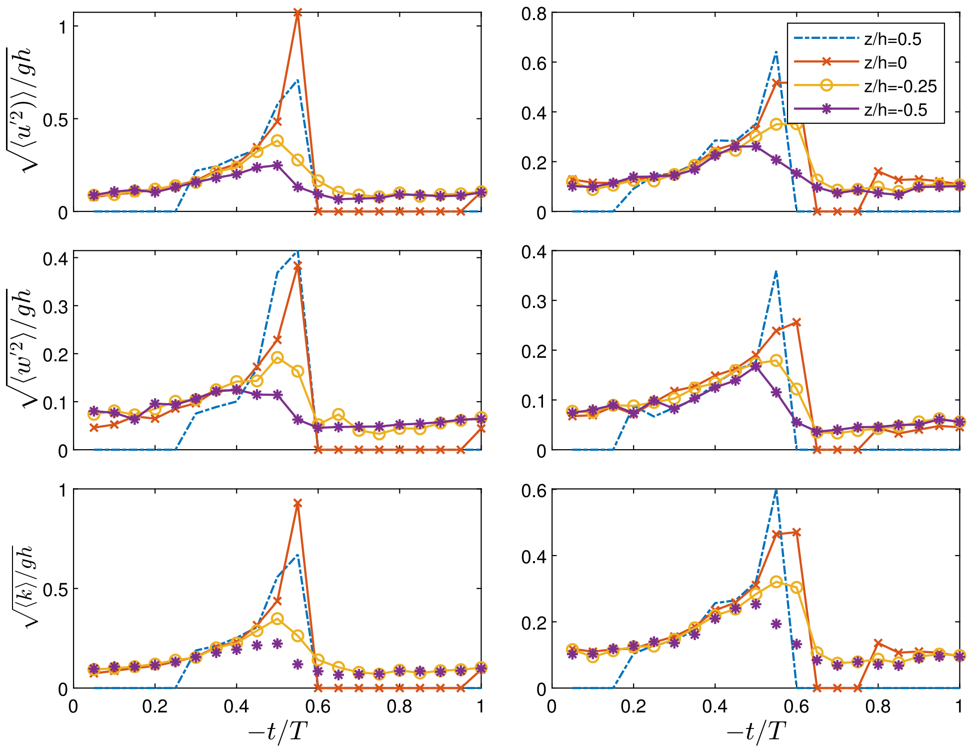

Fig. 17. Phase-averaged turbulence intensities and turbulent kinetic energy as function of $-t/T$ at center positions P5 (left column) and P6 (right column). Turbulence data for z/h equal to (dashed line) 0.5, (crosses) 0, (circles) −0.25 and (stars) −0.5 are presented.

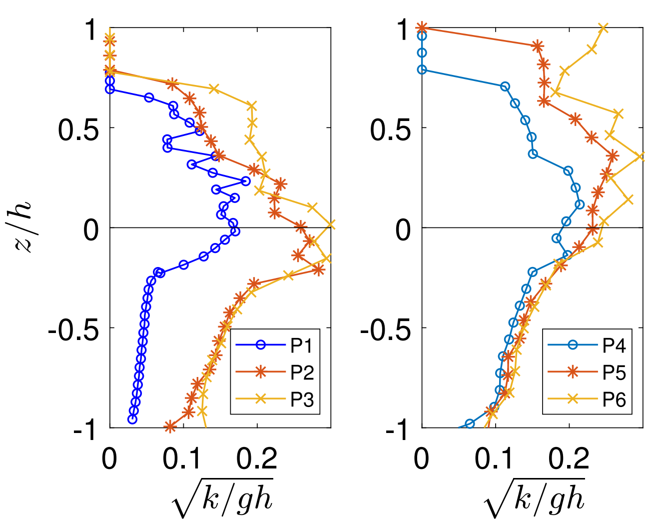

Fig. 18. Time-averaged TKE at positions P1 to P6.

will see later, that these wave shear stresses are comparable to and in some case significantly larger in magnitude compared to the turbulent shear stresses.

3.4. Turbulence intensities, TKE and shear stress

We will now examine the turbulence characteristics by discussing the phase-averaged turbulence intensities and turbulent kinetic energy (TKE) as a function of time $-t/T$ first. This will then be followed by the time-averaged turbulence intensities and turbulent kinetic energy (TKE) and the turbulent shear stress.

Figs. 15 to 17 shows plots of the phase-averaged turbulence intensities and turbulent kinetic energy (TKE), as a function of time $-t/T$, at various depths at each position P1 to P6. These plots are extracted from the phase ensembled turbulence data over each measurement section in similar fashion to the flowfields described/presented in the previous section. Peak values are seen to occur in the crests of the wave at $-t/T \sim 0.5$. The turbulence levels then decay in the trough region following the wave crest. The highest values occurring at a depth $z/h \approx 0$, i.e. at the toe of the wave front. Peak turbulence below the trough levels occurs slightly later in phase compared to levels above the trough level. Over the trough region all quantities seem to have a uniform level over a wide range of $-t/T$ values, the Froude scaled TKE typically has a value of 0.1 at a depth z/h=−0.5. The peak values of TKE can be as high as 1 at the toe of the wave. It is clear from these plots that this plunging wave results in a massive injection of turbulence in the breaking region of the wave. The turbulence is then convected/diffused to lower vertical positions and spreads through out the wave. Further,

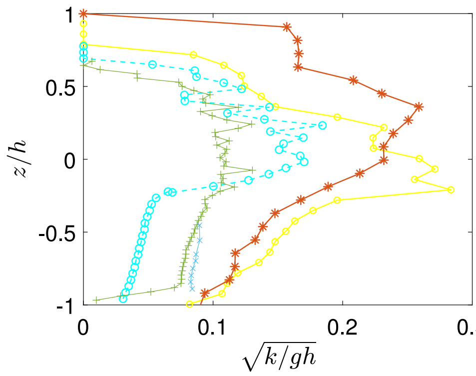

Fig. 19. Time-averaged TKE at position P1 ($h/h_b = 0.846$) (cyan circles), P3 ($h/h_b = 0.643$) (red *) and P5 ($h/h_b = 0.444$) (yellow circles) together TKE measurements by Govender et al. (2002) ($h/h_b = 0.756$) (green +) and Ting and Kirby (1994) ($h/h_b = 0.675$) (blue x).

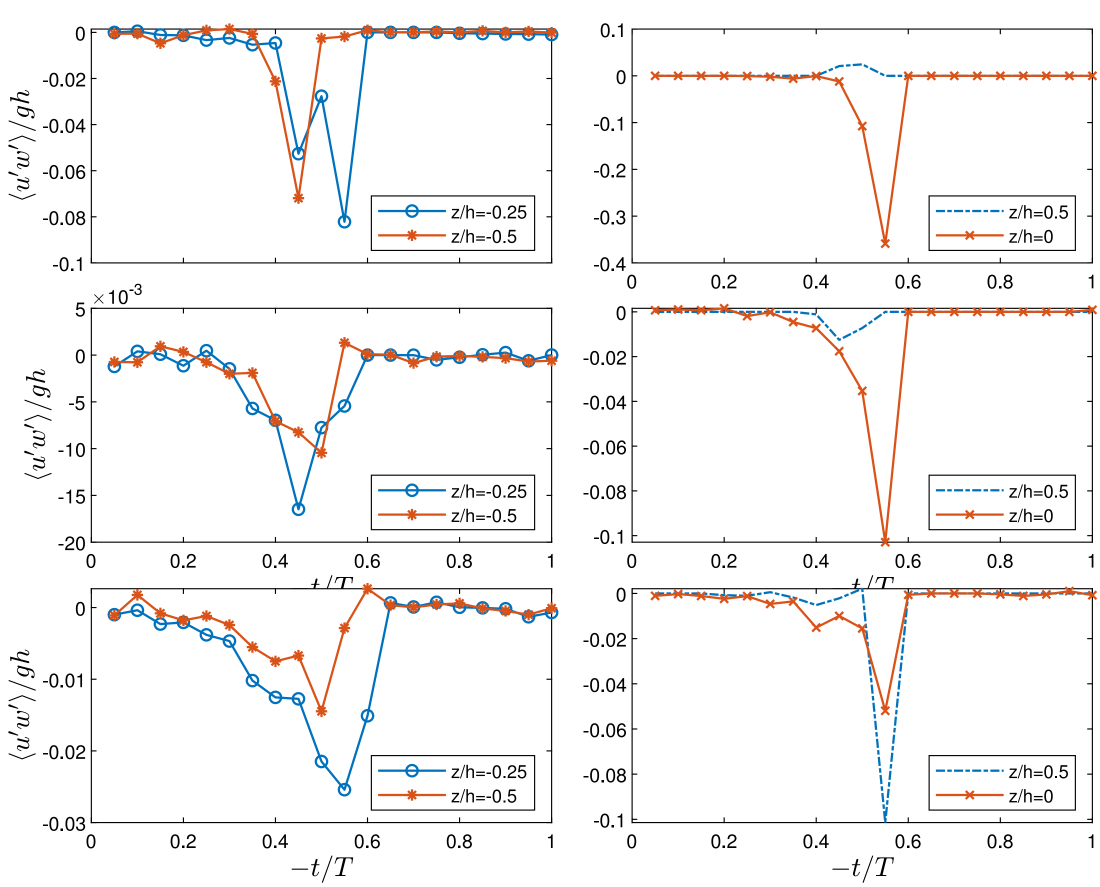

Fig. 20. Turbulence shear stress $\langle u'w'\rangle$ at position P2 (top row), P4 (middle row) and P6 (bottom row), as function of phase for z/h=−.5, −0.25, 0 and 0.5.

due to the intensity of wave breaking and the shorter wave period, the turbulence does not have sufficient time to decay before the next wave crest appears. This uniform turbulence levels below the trough level is due to the high levels of vortices generated by this wave and the variability of the vortex motion which results in smoothing of the turbulence across the wave phase in the trough regions. The leveling of the turbulence in the trough region has also been observed by Liiv (2001) who conducted experiments on a mild 2 s period plunging wave. In comparison with the turbulence intensities occurring in the wave crests, the intensities closer to the bottom are almost uniform across the wave. This could have implications in sediment modeling were a time-averaged approached would seem adequate, especially in the inner surf zone.

Fig. 18 shows the time-averaged turbulent kinetic energies at positions P1 to P6. The high levels of TKE seen in the phase-averaged plots also shows up clearly here. Near the bottom, the Froude scaled TKE is approximately 0.1 for positions P2 to P6 and this increases up the water column. Peak values of the Froude scaled TKE exceeds 0.2 above the trough level in most cases.

The Froude scaled TKE measurements by Ting and Kirby (1994) and those of Govender et al. (2002), together with the present measurements at positions P1, P3 and P5 are shown in Fig. 19. Near the bed our measurements are approximately 25% higher than those of Ting and Kirby (1994) and Govender et al. (2002). In the Ting and Kirby case waves of 5 s period were used and this period was long enough for the turbulence to decay before the next crests appears, thus giving a lower time averaged TKE below the trough level. This is opposite to what happens in the present experiment. Above the trough level TKE in the present experiment are also higher than those reported by Govender et al. (2002).

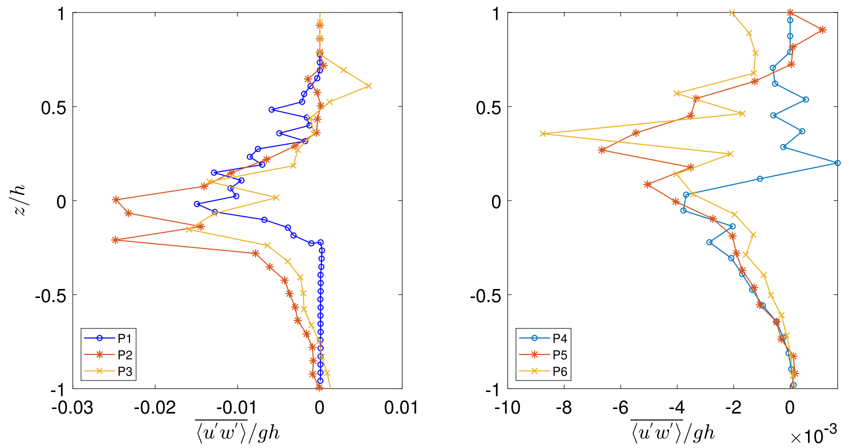

Fig. 21. Time-average turbulence shear stress $\overline{\langle u'w' \rangle}/gh$ at positions P1 to P6.

Fig. 20 shows plots of the phase-averaged turbulent shear stress (TSS) $\langle u'w' \rangle$, scaled by $\sqrt{gh}$, as a function of time $-t/T$, at various depths at each of the positions P2, P4 and P6. Peak values of shear occur in the crests and decaying with depth. The shear stress also reduces in magnitude as the wave passes. At P2 the shear is confined mainly under the crest and decays rapidly as the wave passes. Further in the surf zone, at P6, the shear decays much more gradually as the wave passes. Peak magnitudes under the crest, for positions below the trough level, are in the range 0.02 to 0.08 at position P2, and 0.01 to 0.025 at position P6. These are similar to those observed by Liiv (2001).

The time averaged turbulence shear stress $\overline{\langle u'w' \rangle}$ is plotted in Fig. 21 (excluding $-\rho$). At station 1 TSS is minimal for positions below the trough level, close to zero through out the water column. As we move across the outer surf zone and into the inner surf zone $\overline{\langle u'w' \rangle}$ is negative through out the water column. It increases from the bottom upwards reaching maximum levels around $z/h \approx 0$ at positions P1 to P3. At positions P4 to P6 maximum negative values of TSS occur higher up the water column. As mentioned previously this TSS levels are comparable to or smaller than the wave shear stress levels reported earlier.

4. Summary and conclusion

This experimental study of a strong plunging wave breaking on a 1:20 slope laboratory beach presents fluid velocities across the outer and inner surf zones, also spanning the entire water column. By using video and bubble imaging techniques, measurements of the fluid velocities in the highly aerated roller region was made possible. The velocities were analyzed to determine the mean and turbulence velocities, and the mean and turbulence shear stresses across the outer and inner surf zones. These analysis revealed a distinct change in the behavior as the breaking wave propagates through the outer and inner surf zones.

The analysis of the instantaneous velocity fields revealed clear large scale vortices generated by the overturning wave present in the outer surf zone through out the wave cycle. The outer zone is the transition zone where the plunging jet impacts the water in front and forming multiple splash-ups generating a few horizontal vortices. These large scale vortices originate in the crest and are convected down into the water column. The analysis of the time-averaged velocities reveal distinct changes in the characteristics of the on-shore and off-shore velocity fluxes in the outer and inner surf zone. The profile of the undertow across the water column in the outer surf zone is also affected by dynamic breaking occurring in the outer zone. The profile changes from that which is typical of non breaking waves near the break-point, increasing from the bottom upwards, to a more uniform distribution across the depth near the inner surf zone which is typical of a undertow profile of a plunging wave in the inner zone. These changes also reveal themselves in the velocity fluxes across the surf zone. The phase relation between the horizontal and vertical mean velocities (which is often neglected in modeling) is found to differ from the usual 45 degree typical of shallow water (Cnoidal type) non-breaking waves. In the outer zone a 180 degrees phase difference was found to occur, while in the inner zone the phase difference was close to zero degrees.

The analysis of the turbulence velocities revealed peak intensities in the crests of the wave. In the outer zone the peak intensities, which have a strong phase dependence, persist throughout the entire water column. This contrasts with measurements in the inner surf zone where it is observed that intensities near the bottom tend to be somewhat smeared out over the wave cycle. Similar features are seen in the plots of the turbulence shear stresses. In the outer surf zone there are rapid changes in turbulence shear stress across the wave phase even for positions near the bottom. Turbulence shear stress observations in the inner surf zone by contrast show less variability over the wave cycle near the bottom. Considering these results in terms of sediment suspension and transport modeling, it is suggested that these observations imply that a time-averaged turbulent closure model may provide reasonable approximations in the inner surf zone. By contrasts a computationally more intensive phase dependent model will likely be required in the outer surf zone.

We envisage that the present set of measurements will supplement existing experimental data for a better understanding of breaker zone flow structures as well as being useful for numerical model validation purposes.

CRediT authorship contribution statement

K. Govender: Conducting experiments and data analysis, Writing – original draft. **R. Mukaro:** Conducting experiments, Editing of manuscript. **G. Mocke:** Data analysis, Editing of manuscript.

Declaration of competing interest

The authors declare that they have no known competing financial interests or personal relationships that could have appeared to influence the work reported in this paper.

Data availability

Data will be made available on request.

Acknowledgements

The experimental aspects of the work described in this paper was supported by the Council for Scientific and Industrial Research by providing financial assistance and access to their research faciltiy in Stellenbosch, South Africa.

References

Van der A, D., van der Zanden, J., O´ Donoghue, T., Hurther, D., Caceres, I., Mclelland, S., Ribberink, J., 2017. Large-scale laboratory study of breaking wave hydrodynamics over a fixed bar. J. Geophys. Res. Oceans 122, 3287–3310.

Basco, D., 1985. A qualitative description of wave breaking. J. Waterway Port Coastal Ocean Eng. 171–188.

Blenkinsopp, C., Chaplin, J., 2007. Void fraction measurements in breaking waves. Proc. R. Soc. 463, 315–3170.

Bonmarin, P., 1989. Geometrical properties of deep water breaking waves. J. Fluid Mech. 209, 405–433.

Chang, K.-A., Liu, P.-F., 1996. Measurements of breaking waves using particle image velocimetry. In: Proc. 25th Int. Conf. Coast. Eng.. pp. 527–537.

Chang, K.-A., Liu, P.-F., 1999. Experimental investigation of turbulence generated by breaking waves in water of intermediate depth. Phys. Fluid 1, 3339–3400.

Cox, D., Kobayashi, N., 2000. Identification of intense, intermittent coherent motion under shoaling and breaking waves. J. Geophys. Res. 105, 14223–14236.

Cox, D., Shin, S., 2003. Laboratory measurements of void fraction an turbulence in the bore region of the surf zone. J. Eng. Mech. 1197–1205.

De Serio, F., Mossa, M., 2006. Experimental study on the hydrodynamics of regular breaking waves. Coast. Eng. 53, 99–113.

Flick, R., Guza, A., Inman, C., 1981. Elevation and velocity measurements of laboratory shoaling waves. J. Geophys. Res. 86, 4149–4160.

Govender, K., Mocke, G., Alport, M., 2002. Video-imaged surf zone wave and roller structures and flowfields. J. Geophys. Res. Oceans 107, 3072.

Govender, K., Mocke, G., Alport, M., 2004. Dissipation of isotropic turbulence and length scale measurements through the wave roller in laboratory spilling waves. J. Geophys. Res. Oceans 109, C08018: 1–8.

Hansen, Y., Blanchat, T., Seeley Jr., C., Canaan, R., 1992. Simultaneous velocity measurements of both components of a two-phase flow using particle image velocimetry. Int. J. Multiph. Flow. 18, 371–395.

Hoque, A., Aoki, S., 2005. Distributions of void fraction under breaking waves in the surf zone. Ocean Eng. 32, 1829–1840.

Hsu, W.Y., Huang, Z.-C., Na, B., Chang, K.A., Chuang, L., Yang, R.Y., 2019. Laboratory observation of turbulence and wave shear stresses under large scale breaking waves over a mild slope. J. Geophys. Res. Oceans 124, 7486–7512.

Huang, Z., Hwung, H., Hsiao, S., Chang, K., 2010. Laboratory obseravtion of boundary layer flow under spilling breakers in surf zone. Coast. Eng. 57, 343–357.

Hwung, H., Chyan, J., Chung, Y., 1992. Energy dissipation and air bubble mixing inside the surf zone. In: Proc. 23rd Int. Conf. Coast. Eng.. pp. 308–321.

Jansen, P., 1986. Laboratory obseravtion of the kinematics in the aerated region of breaking waves. Coast. Eng. 9, 453–477.

Kimmoun, O., Branger, H., 2007. A particle image velocimetry investigation on laboratory surf-zone breaking waves over a sloping beach. J. Fluid Mech. 588, 353–397.

Lakehal, D., Liovic, P., 2011. Turbulence structure and interaction with steep breaking waves. J. Fluid Mech. 674, 522–577.

Liiv, T., 2001. Investigation of turbulence in a plunging breaking wave. Proc. Estonian Acad. Sci. Eng. 7, 58–78.

Liiv, T., Lagemaa, P., 2008. Variation of the velocity and turbulent kinetic energy field in the wave in the vicinity of the breakpoint. Estonian J. Eng. 14, 42–64.

Longo, S., 2009. Vorticity and intermittency within the pre-breaking region of spilling breakers. Coast. Eng. 56, 285–296.

Ma, G., Shi, F., Kirby, J., 2011. A polydisperse two-fluid model for surf zone bubble simulation. J. Geophys. Res. 116, 05010. http://dx.doi.org/10.1029/2010JC006667.

Mocke, G., 2001. Structure and modelling of surf zone turbulence due to wave breaking. J. Geophys. Res. Oceans 106, 17039–17057.

Mori, N., Sukuzi, T., kakuno, S., 2007. Experimental study of air bubbles and turbulence characteristics in the surf zone. J. Geophys. Res. Oceans 112 doi:10.1029/2006JC003647, C05014.

Na, B.-J., Chang, K.-A., Huang, Z.-C., Hsu, W.-Y., 2018. Large scale laboratory observation of flow properties in plunging breaking waves. Coastal Eng. 138, 66–79.

Na, B.J., Chang, K.-A., Huang, Z.C., Lim, H.-J., 2016. Turbulent flow field and air entrainment in laboratory plunging breaking waves. J. Geophys. Res. Oceans 121, 2980–3009.

Nadaoka, K., Kondoh, T., 1982. Laboratory measurement of velocity field structure in the surf zone by LDV. Coastal Eng. Jpn. 25, 125–146.

Pedrozo-Acuña, A., Silva, R., 2011. Laboratory investigation of pressure gradients induced by plunging breakers. Coastal Eng. 58, 722–738.

Rojas, G., Loewen, M., 2010. Void fraction measurements beneath plunging and spilling breaking waves. J. Geophys. Res. 115, C08001. http://dx.doi.org/10.1029/2009JC005614.

Ryu, Y., Chang, K., Lim, H., 2005. Use of bubble image velocimetry for measurement of plunging wave impinging on structure and associated greenwater. Meas. Sci. Technol. 16, 1945–1953.

Sou, I., Cowen, E., Liu, P.-F., 2010. Evolution of the turbulence structures in the surf zone and swash zones. J. Fluid Mech. 644, 193–216.

Stansby, P., Feng, T., 2005. Kinematics and depth-integrated terms in surf zone waves from laboratory measurement. J. Fluid Mech. 279–310.

Stive, M., 1980. Velocity and pressure fields in spilling breakers. In: 17th Int. Conf. Coastal Eng.. pp. 547–566.

Ting, F., 2013. Laboratory measurements of large-scale near-bed turbulent flow structures under plunging regular waves. Coast. Eng. 77, 120–139.

Ting, F., Kirby, J., 1994. Observation of undertow and turbulence in a laboratory surf zone. Coast. Eng. 24, 51–80.

Ting, F., Kirby, J.T., 1995. Dynamics of surf-zone turbulence in strong plunging breaker. Coast. Eng. 24, 177–204.

Ting, F., Reimnitz, J., 2015. Volumetric velocity measurements of turbulent coherent structures induced by plunging regular waves. Coastal Eng. 104, 93–112.

Watanabe, Y., Saeki, H., Hosking, R., 2005. Three-dimensional vortex structures under breaking waves. J. Fluid Mech. 545, 291–328.